submitted to *Geophys. J. Int.*

Revealing transient strain in geodetic data with Gaussian process regression

T. T. Hines[1] and E. A. Hetland[1]

[1] *Department of Earth and Environmental Sciences, University of Michigan, Ann Arbor, MI, USA*

SUMMARY

Transient strain rates derived from GNSS data can be used to detect and understand geophysical phenomena such as slow slip events and postseismic deformation. Here we propose using Gaussian process regression (GPR) as a tool for estimating transient strain rates from GNSS data. GPR is a non-parametric, Bayesian method for interpolating scattered data. Transient strain rates estimated with GPR have meaningful uncertainties, allowing geophysical signal to be easily discerned from noise. In our approach, we assume a stochastic prior model for transient displacements. The prior describes how much one expects transient displacements to covary spatially and temporally. A posterior estimate of transient strain rates is obtained by differentiating the posterior displacements. One limitation with GPR is that it is not robust against outliers, so we introduce a pre-processing method for detecting and removing outliers in GNSS data. As a demonstration, we use GPR to detect transient strain resulting from slow slip events in the Pacific Northwest. Maximum likelihood methods are used to constrain a prior model for transient displacements in this region. The temporal covariance of our prior model is described by a compact Wendland covariance function, which significantly reduces the computational burden that can be associated with GPR. Our results reveal the spatial and temporal evolution of strain from slow slip events. We verify that the transient strain estimated with GPR is in fact geophysical signal by comparing it to the seismic tremor that is associated with Pacific Northwest slow slip events.

Key words: XXX – XXX – XXX – XXX.

1 INTRODUCTION

Crustal strain rates are fundamentally important quantities for assessing seismic hazard. Knowing where and how quickly strain is accumulating gives insight into where we can expect stored elastic energy to be released seismically. Consequently, secular crustal strain rates estimated from GNSS data have been used to constrain seismic hazard models such as UCERF3 (Field et al. 2014). Transient crustal strain, which is caused by geophysical phenomena such as slow slip events (SSEs) or postseismic deformation, is also relevant for assessing seismic hazard. While transient strain itself is not damaging, there is a risk that it can trigger major earthquakes (Roeloffs 2006; Freed & Lin 2001). Dense networks of continuous GNSS stations, such as the Plate Boundary Observatory (PBO), make it possible to identify transient strain with high fidelity. Developing and improving upon methods for deriving secular and transient strain from GNSS data is an active area of research.

Most methods for estimating strain rates from GNSS data assume some parametric form for the deformation signal. The simplest method for estimating secular strain rates assumes that GNSS derived velocities can be described with a first-order polynomial (i.e, the deformation gradients are constant) over some subnetwork of the GNSS stations (e.g., Feigl et al. 1990; Murray & Lisowski 2000). The components of the strain rate tensor for each subnetwork are then determined from the least squares fit to the observations. The assumption that deformation gradients are spatially uniform is not appropriate when subnetworks span too large of an area. To help overcome this deficiency, Shen et al. (1996, 2015) used an inverse distance weighting scheme, in which the estimated strain rate at a point is primarily controlled by observations at nearby stations. The method of Shen et al. (1996, 2015) can be viewed as a form of local least squares regression with a first-order polynomial (e.g., Hastie et al. 2009, sec. 6). Other methods for estimating secular strain rates have parameterized GNSS derived velocities with bi-cubic splines (Beavan & Haines 2001), spherical wavelets (Tape et al. 2009), and elastostatic Green's functions (Sandwell & Wessel 2016). The type of basis functions and the number of degrees of freedom for a parameterization, which are often chosen subjectively, have a strong influence on the strain solution. If there are too few degrees of freedom in the parameterization, then estimated strain rates will be biased and the uncertainties will be underestimated. On the other hand, if there are too many degrees of freedom, then there will not be any coherent features in the estimated strain rates. The methods described by Beavan & Haines (2001) and Tape et al. (2009) also require the user to specify penalty parameters that control a similar trade-off between bias and variance in the solution. One could parameterize deformation with a physically motivated model of interseismic deformation (e.g., Meade & Hager 2005; McCaffrey et al. 2007). In such models the lithospheric rheology and fault geometries are assumed to be known. Any errors in the assumed physical model could result in biased strain estimates and underestimated formal uncertainties.

The aforementioned studies are concerned with estimating secular strain rates. In recent years the Southern California Earthquake Center (SCEC) community has shown interest in developing methods for detecting transient strain. SCEC supported a transient detection exercise (Lohman & Murray 2013), where several research groups tested their methods for detecting transient geophysical signal with a synthetic GNSS dataset. Among the methods tested were the Network Strain Filter (NSF) (Ohtani et al. 2010) and the Network Inversion Filter (NIF) (Segall & Mathews 1997). The NSF uses a wavelet parameterization to describe the spatial component of geophysical signal. The NIF, which is intended for imaging slow fault slip from geodetic data, uses the elastic dislocation Green's functions from Okada (1992). For the NSF and NIF, the time dependence of the geophysical signal is modeled as integrated Brownian motion. The method described in Holt & Shcherbenko (2013) was also tested in the SCEC transient detection exercise, which calculates strain rates using a bi-cubic spatial parameterization of displacements between time epochs. Holt & Shcherbenko (2013) defined a detection threshold based on the strain rate magnitude, and below we demonstrate that this is indeed an effective criterion for identifying geophysical signal. For the same reasons descibed above, the transient deformation and corresponding uncertainties estimated by these methods can be biased by the chosen spatial parameterization. It is then difficult to distinguish signal from noise with these methods, which limits their utility for transient detection.

Here we propose using Gaussian process regression (GPR) (Rasmussen & Williams 2006) to estimate transient strain from GNSS data. GPR is closely related to kriging (Cressie 1993) and least squares collocation (Moritz 1978). The latter has been used by Kato et al. (1998) and El-Fiky & Kato (1998) to estimate secular strain rates from GNSS data. GPR is a Bayesian, non-parametric method for inferring a continuous signal from scattered data. Since GNSS stations are irregularly spaced and observation times may differ between stations, GPR is an ideal tool for synthesizing discrete GNSS data into a spatially and temporally continuous representation of surface deformation. GPR is Bayesian in that we describe our prior understanding of the geophysical signal with a Gaussian process. A Gaussian process is a continuous stochastic process whose value at any collection of points can be described as a Gaussian random vector. Just as a Gaussian random vector is fully determined by a mean vector and a covariance matrix, a Gaussian process is fully determined by a mean function and a covariance function. For example, Brownian motion, $B(t)$, is a well known Gaussian process in $\mathbb{R}^1$ which has the mean function $\mathrm{E}[B(t)] = 0$ and the covariance function $\mathrm{Cov}\left[B(t), B(t')\right] = \min(t, t')$, where $t, t' \geq 0$. If there is no information available to help choose an appropriate prior Gaussian process, then maximum likelihood methods can be used to objectively choose one that is most consistent with the data. Once a prior is selected, we incorporate GNSS observations with the prior to form a posterior estimate of transient strain. The posterior transient strain is also a Gaussian process, and we can use its distribution to confidently discern geophysical signal from noise. We use GPR to infer strain resulting from SSEs in the Pacific Northwest, demonstrating that GPR is an effective tool for detecting transient geophysical processes.

2 ESTIMATING TRANSIENT STRAIN RATES

We seek a spatially and temporally dependent estimate of transient strain rates. We consider transient strain rates to be any deviation from secular strain rates, and our attention is limited to horizontal strain rates. We denote transient strain rates as $\dot{\varepsilon}(p)$, where p represents the ordered pair $(\vec{x}, t)$, $\vec{x} = (x_\mathrm{e}, x_\mathrm{n})$ are spatial coordinates, and t is time. For simplicity, we assume that the study region is sufficiently small that $\vec{x}$ can be considered a point in a 2-D map projection that is aligned with the cardinal directions. We determine $\dot{\varepsilon}$ by spatially and temporally differentiating estimates of transient displacements, $\vec{u}(p) = (u_\mathrm{e}(p), u_\mathrm{n}(p))$.

We make a prior assumption that each component of $\vec{u}$ is a Gaussian process with zero mean and a generic covariance function $\mathrm{Cov}\left[u_i(p), u_i(p')\right] = C_{u_i}(p, p')$. Using a more concise notation, we write our prior on each component of $\vec{u}$ as $u_i \sim \mathcal{GP}\left(0, C_{u_i}\right)$. The function C_{u_i} must be positive definite in order to be a valid covariance function. By definition, C_{u_i} is a positive definite function if the matrix $\left[C_{u_i}(p, p')\right]_{(p,p') \in \boldsymbol{P} \times \boldsymbol{P}}$ is positive definite for any set of points $\boldsymbol{P}$ (Cressie 1993, sec. 2.5). We assume that C_{u_i} can be separated into spatial and temporal functions as

$$C_{u_i}(p, p') = C_{u_i}\big((\vec{x}, t), (\vec{x}', t')\big) = X_i(\vec{x}, \vec{x}')T_i(t, t'). \tag{1}$$

As long as the functions X_i and T_i are positive definite, C_{u_i} is guaranteed to also be positive definite (Rasmussen & Williams 2006, sec. 4.2.4). We also require that the derivatives $\partial^2 X_i(\vec{x}, \vec{x}')/\partial x_j \partial x'_j$ and $\partial^2 T_i(t, t')/\partial t \partial t'$ exist. This ensures that $\vec{u}$ is spatially and temporally differentiable, allowing us to compute $\dot{\varepsilon}$ (See Adler (1981, sec. 2.2) or Papoulis (1991, sec. 10A) for a definition of stochastic differentiation and the conditions for differentiability). As an example, we can satisfy our requirements for positive definiteness and differentiability by using a squared exponential function for X_i and T_i,

$$X_i(\vec{x}, \vec{x}') = \exp\left(\frac{-||\vec{x} - \vec{x}'||_2^2}{2\ell^2}\right), \quad T_i(t, t') = \phi^2 \exp\left(\frac{-|t - t'|^2}{2\tau^2}\right). \tag{2}$$

The parameters ℓ and τ control the length-scale and time-scale, respectively, of realizations of u_i.

The parameter ϕ, which we have arbitrarily chosen to incorporate into T_i rather than X_i, controls the amplitude of realizations of u_i (Figure XXX). While the squared exponential function is a commonly used covariance function for GPR, it is not appropriate for every application. The appropriate choice for X_i and T_i may vary depending on the geophysical signal we are trying to describe. To keep this section sufficiently general, we hold off on specifying X_i and T_i until Section 3.2, where we estimate transient strain from slow slip events in the Pacific Northwest.

GNSS data records transient displacements as well as other physical and non-physical processes that we are not interested in. We first consider component i of a single GNSS displacement observation made at station j, which is located at $\vec{x}^{(j)}$, and time $t^{(k)}$. We describe this observation, $d_i^{*(jk)}$, as a realization of the random variable

$$\begin{aligned} d_i^{(jk)} =& u_i\left(\vec{x}^{(j)}, t^{(k)}\right) + \eta_i^{(jk)} + a_i^{(j)} + b_i^{(j)} t^{(k)} + \\ & c_i^{(j)} \sin\left(2\pi t^{(k)}\right) + e_i^{(j)} \cos\left(2\pi t^{(k)}\right) + \\ & f_i^{(j)} \sin\left(4\pi t^{(k)}\right) + g_i^{(j)} \cos\left(4\pi t^{(k)}\right), \end{aligned} \tag{3}$$

where $\eta_i^{(jk)}$ describes noise, $a_i^{(j)}$ is an offset that is unique for each station, $b_i^{(j)}$ is the secular velocity at $\vec{x}^{(j)}$, and the sinusoids describe seasonal deformation (using units of years for $t^{(k)}$). We then consider the column vector of n GNSS displacement observations, $\boldsymbol{d}_i^*$, where the subscript indicates that we are still only considering component i of displacements. The observations are made at m stations, and the times and positions for each observation are described by the set $\boldsymbol{P}$. $\boldsymbol{d}_i^*$ can be considered a realization of the random vector $\boldsymbol{d}_i$, which is formed by evaluating eq. (3) at each point in $\boldsymbol{P}$. To write out $\boldsymbol{d}_i$ explicitly, we let $\boldsymbol{G}$ be an $n \times 6m$ matrix consisting of the basis functions from eq. (3) (i.e., the linear trends and sinusoids for each station) evaluated at each point in $\boldsymbol{P}$. The coefficients corresponding to each basis function are collected into the column vector $\boldsymbol{m}_i$. The noise for all the observations are described by the column vector $\boldsymbol{\eta}_i$. We can then write $\boldsymbol{d}_i$ as

$$\boldsymbol{d}_i = u_i(\boldsymbol{P}) + \boldsymbol{\eta}_i + \boldsymbol{G}\boldsymbol{m}_i, \tag{4}$$

where the notation $u_i(\boldsymbol{P})$ represents the column vector $[u_i(p)]_{p\in\boldsymbol{P}}$.

We assume a diffuse prior for the components of $\boldsymbol{m}_i$, that is to say $\boldsymbol{m}_i \sim \mathcal{N}(\boldsymbol{0}, \kappa^2\boldsymbol{I})$ in the limit as $\kappa \to \infty$. Of course, the secular velocities, $b_i^{(j)}$, are spatially correlated and we could invoke a tectonic model to form a prior on $b_i^{(j)}$. However, in our application to the Pacific Northwest, we will be using displacement time series which are long enough to sufficiently constrain $b_i^{(j)}$ for each station, avoiding the need to incorporate a prior. Likewise, seasonal deformation is spatially correlated (Dong et al. 2002; Langbein 2008), and it may be worth exploring and exploiting such a correlation in a future study. We assume that $\boldsymbol{\eta}_i$ is a spatially and/or temporally correlated random vector distributed as

$\mathcal{N}(\mathbf{0}, \boldsymbol{C}_{\eta_i})$. For example, $\boldsymbol{\eta}_i$ can be uncorrelated white noise, temporally correlated noise describing benchmark wobble (e.g., Wyatt 1982, 1989), and/or spatially correlated noise describing common mode error (e.g., Wdowinski et al. 1997). The appropriate noise model may vary depending on the application, and we hold off on specifying the covariance matrix, $\boldsymbol{C}_{\eta_i}$, until Section 3.1. We are now able to write the distribution of $\boldsymbol{d}_i$ as

$$\boldsymbol{d}_i \sim \mathcal{N}\left(\mathbf{0}, C_{u_i}(\boldsymbol{P},\boldsymbol{P}) + \boldsymbol{C}_{\eta_i} + \kappa^2 \boldsymbol{G}\boldsymbol{G}^T\right), \tag{5}$$

where $C_{u_i}(\boldsymbol{P},\boldsymbol{P})$ represents the matrix $[C_{u_i}(p,p')]_{(p,p')\in\boldsymbol{P}\times\boldsymbol{P}}$.

We form a posterior estimate of transient displacements, denoted as $\hat{u}_i$, by updating u_i with the fact that $\boldsymbol{d}_i^*$ was realized from the random vector $\boldsymbol{d}_i$, that is to say $\hat{u}_i = u_i|(\boldsymbol{d}_i = \boldsymbol{d}_i^*)$. A general solution for $\hat{u}_i$ is derived in von Mises (1964, sec. 8.9), where we find that $\hat{u}_i$ is distributed as $\mathcal{GP}(\mu_{\hat{u}_i}, C_{\hat{u}_i})$ with mean function

$$\begin{aligned}
\mu_{\hat{u}_i}(p) &= \mathrm{E}\left[u_i(p)\right] + \mathrm{Cov}\left[u_i(p), \boldsymbol{d}_i\right] \mathrm{Cov}\left[\boldsymbol{d}_i\right]^{-1} \left(\boldsymbol{d}_i^* - \mathrm{E}\left[\boldsymbol{d}_i\right]\right) \\
&= C_{u_i}(p,\boldsymbol{P}) \left(C_{u_i}(\boldsymbol{P},\boldsymbol{P}) + \boldsymbol{C}_{\eta_i} + \kappa^2 \boldsymbol{G}\boldsymbol{G}^T\right)^{-1} \boldsymbol{d}_i^*
\end{aligned} \tag{6}$$

and covariance function

$$\begin{aligned}
C_{\hat{u}_i}(p,p') &= \mathrm{Cov}\left[u_i(p), u_i(p')\right] - \mathrm{Cov}\left[u_i(p), \boldsymbol{d}_i\right] \mathrm{Cov}\left[\boldsymbol{d}_i\right]^{-1} \mathrm{Cov}\left[\boldsymbol{d}_i, u_i(p')\right] \\
&= C_{u_i}(p,p') - C_{u_i}(p,\boldsymbol{P}) \left(C_{u_i}(\boldsymbol{P},\boldsymbol{P}) + \boldsymbol{C}_{\eta_i} + \kappa^2 \boldsymbol{G}\boldsymbol{G}^T\right)^{-1} C_{u_i}(\boldsymbol{P},p').
\end{aligned} \tag{7}$$

However, we are interested in the limit as $\kappa \to \infty$, and the form for eqs. (6) and (7) is not suitable for evaluating this limit. We use a partitioned matrix inversion identity (Press et al. 2007, sec. 2.7.4) to rewrite eqs. (6) and (7) as

$$\mu_{\hat{u}_i}(p) = \begin{bmatrix} C_{u_i}(p,\boldsymbol{P}) & \mathbf{0} \end{bmatrix} \begin{bmatrix} C_{u_i}(\boldsymbol{P},\boldsymbol{P}) + \boldsymbol{C}_{\eta_i} & \boldsymbol{G} \\ \boldsymbol{G}^T & -\kappa^{-2}\boldsymbol{I} \end{bmatrix}^{-1} \begin{bmatrix} \boldsymbol{d}_i^* \\ \mathbf{0} \end{bmatrix} \tag{8}$$

and

$$\begin{aligned}
C_{\hat{u}_i}(p,p') = C_{u_i}(p,p') - \\
\begin{bmatrix} C_{u_i}(p,\boldsymbol{P}) & \mathbf{0} \end{bmatrix} \begin{bmatrix} C_{u_i}(\boldsymbol{P},\boldsymbol{P}) + \boldsymbol{C}_{\eta_i} & \boldsymbol{G} \\ \boldsymbol{G}^T & -\kappa^{-2}\boldsymbol{I} \end{bmatrix}^{-1} \begin{bmatrix} C_{u_i}(\boldsymbol{P},p') \\ \mathbf{0} \end{bmatrix}.
\end{aligned} \tag{9}$$

Taking the limit as $\kappa \to \infty$, we get the solution for the mean and covariance of $\hat{u}_i$,

$$\mu_{\hat{u}_i}(p) = \begin{bmatrix} C_{u_i}(p,\boldsymbol{P}) & \mathbf{0} \end{bmatrix} \begin{bmatrix} C_{u_i}(\boldsymbol{P},\boldsymbol{P}) + \boldsymbol{C}_{\eta_i} & \boldsymbol{G} \\ \boldsymbol{G}^T & \mathbf{0} \end{bmatrix}^{-1} \begin{bmatrix} \boldsymbol{d}_i^* \\ \mathbf{0} \end{bmatrix} \tag{10}$$

and

$$C_{\hat{u}_i}(p,p') = C_{u_i}(p,p') - \left[\begin{array}{cc} C_{u_i}(p,\boldsymbol{P}) & \mathbf{0} \end{array}\right] \left[\begin{array}{cc} C_{u_i}(\boldsymbol{P},\boldsymbol{P}) + \boldsymbol{C}_{\eta_i} & \boldsymbol{G} \\ \boldsymbol{G}^T & \mathbf{0} \end{array}\right]^{-1} \left[\begin{array}{c} C_{u_i}(\boldsymbol{P},p') \\ \mathbf{0} \end{array}\right]. \quad (11)$$

To ensure that the inverse matrices in eqs. (10) and (11) exist, each column in $\boldsymbol{G}$ must be linearly independent. This condition tends to be violated when there are too few observations at a station. In that case, a singular value decomposition can be used to remove linearly dependent components from $\boldsymbol{G}$.

It should be noted that we have ignored any covariances between the easting and northing components of $\vec{u}$ and $\vec{\boldsymbol{d}}$. This simplification reduces the computational complexity of evaluating the posterior transient displacements because each component can be evaluated independently. However, we are inherently assuming that the principle axes describing the distribution of $\vec{u}(p)$ and $\vec{d}^{(jk)}$ are aligned with the cardinal directions, which is admittedly an arbitrary assumption.

The posterior transient displacements are spatially and temporally continuous, and we can use eqs. (10) and (11) to evaluate $\hat{u}_i$ at any p. Furthermore, $\hat{u}_i$ is spatially and temporally differentiable, allowing us to formulate $\dot{\varepsilon}$ at any p that we may be interested in. The components of $\dot{\varepsilon}$ can be written as

$$\dot{\varepsilon}_{ij}(p) = \frac{1}{2}\frac{\partial}{\partial t}\left(\frac{\partial \hat{u}_i(p)}{\partial x_j} + \frac{\partial \hat{u}_j(p)}{\partial x_i}\right). \quad (12)$$

Since eq. (12) is a linear operation on the Gaussian processes $\hat{u}_i$ and $\hat{u}_j$, we know that $\dot{\varepsilon}_{ij}$ is also a Gaussian process. From Papoulis (1991, sec. 10), we find that the mean and covariance functions for $\dot{\varepsilon}_{ij}$ are

$$\mu_{\dot{\varepsilon}_{\mathrm{ee}}}(p) = \frac{\partial^2 \mu_{\hat{u}_{\mathrm{e}}}(p)}{\partial t\,\partial x_{\mathrm{e}}} \quad (13)$$

$$\mu_{\dot{\varepsilon}_{\mathrm{nn}}}(p) = \frac{\partial^2 \mu_{\hat{u}_{\mathrm{n}}}(p)}{\partial t\,\partial x_{\mathrm{n}}} \quad (14)$$

$$\mu_{\dot{\varepsilon}_{\mathrm{en}}}(p) = \frac{1}{2}\frac{\partial}{\partial t}\left(\frac{\partial \mu_{\hat{u}_{\mathrm{e}}}(p)}{\partial x_{\mathrm{n}}} + \frac{\partial \mu_{\hat{u}_{\mathrm{n}}}(p)}{\partial x_{\mathrm{e}}}\right) \quad (15)$$

and

$$C_{\dot{\varepsilon}_{\mathrm{ee}}}(p,p') = \frac{\partial^4 C_{\hat{u}_{\mathrm{e}}}(p,p')}{\partial t\,\partial t'\,\partial x_{\mathrm{e}}\,\partial x'_{\mathrm{e}}} \quad (16)$$

$$C_{\dot{\varepsilon}_{\mathrm{nn}}}(p,p') = \frac{\partial^4 C_{\hat{u}_{\mathrm{n}}}(p,p')}{\partial t\,\partial t'\,\partial x_{\mathrm{n}}\,\partial x'_{\mathrm{n}}} \quad (17)$$

$$C_{\dot{\varepsilon}_{\mathrm{en}}}(p,p') = \frac{1}{4}\frac{\partial^2}{\partial t\,\partial t'}\left(\frac{\partial^2 C_{\hat{u}_{\mathrm{e}}}(p,p')}{\partial x_{\mathrm{n}}\,\partial x'_{\mathrm{n}}} + \frac{\partial^2 C_{\hat{u}_{\mathrm{n}}}(p,p')}{\partial x_{\mathrm{e}}\,\partial x'_{\mathrm{e}}}\right), \quad (18)$$

respectively.

2.1 Transient detection criterion

Our motivation for estimating transient strain rates is, in part, to detect geophysical phenomena. As we will see, geophysical signal can be easily identified by visually inspecting the solution for $\dot{\varepsilon}$ from eqs. (13) and (16). However, if we want to detect geophysical phenomena automatically, then we need to define a detection criterion. We use a signal-to-noise ratio, SNR, that is based on the Frobenius norm of $\dot{\varepsilon}$, $||\dot{\varepsilon}||_{\mathrm{F}} = \left(\dot{\varepsilon}_{\mathrm{ee}}^2 + \dot{\varepsilon}_{\mathrm{nn}}^2 + 2\dot{\varepsilon}_{\mathrm{en}}^2\right)^{\frac{1}{2}}$, for our detection criterion. In the geodetic literature, $||\dot{\varepsilon}||_{\mathrm{F}}$ is often used as a metric for the strain rate "magnitude", and it is sometimes referred to as the second invariant of strain rate. Noting that $||\dot{\varepsilon}||_{\mathrm{F}}$ is a random variable, we take SNR to be the ratio of the estimated mean and standard deviation of $||\dot{\varepsilon}||_{\mathrm{F}}$. An estimate of the mean is found by evaluating $||\dot{\varepsilon}||_{\mathrm{F}}$ at the mean of $\dot{\varepsilon}$,

$$\begin{aligned} \mu_{||\dot{\varepsilon}||_{\mathrm{F}}} &\approx ||\dot{\varepsilon}||_F\Big|_{\dot{\varepsilon}=\mu_{\dot{\varepsilon}}} \\ &= \left(\mu_{\dot{\varepsilon}_{\mathrm{ee}}}^2 + \mu_{\dot{\varepsilon}_{\mathrm{nn}}}^2 + 2\mu_{\dot{\varepsilon}_{\mathrm{en}}}^2\right)^{\frac{1}{2}}, \end{aligned} \tag{19}$$

and we use nonlinear uncertainty propagation to estimate the standard deviation,

$$\sigma_{||\dot{\varepsilon}||_{\mathrm{F}}} \approx \left(\left(\frac{\partial ||\dot{\varepsilon}||_{\mathrm{F}}}{\partial \dot{\varepsilon}_{\mathrm{ee}}}\Bigg|_{\dot{\varepsilon}=\mu_{\dot{\varepsilon}}} \right)^2 \sigma_{\dot{\varepsilon}_{\mathrm{ee}}}^2 + \left(\frac{\partial ||\dot{\varepsilon}||_{\mathrm{F}}}{\partial \dot{\varepsilon}_{\mathrm{nn}}}\Bigg|_{\dot{\varepsilon}=\mu_{\dot{\varepsilon}}} \right)^2 \sigma_{\dot{\varepsilon}_{\mathrm{nn}}}^2 + \left(\frac{\partial ||\dot{\varepsilon}||_{\mathrm{F}}}{\partial \dot{\varepsilon}_{\mathrm{en}}}\Bigg|_{\dot{\varepsilon}=\mu_{\dot{\varepsilon}}} \right)^2 \sigma_{\dot{\varepsilon}_{\mathrm{en}}}^2 \right)^{\frac{1}{2}}, \tag{20}$$

where $\sigma_{\dot{\varepsilon}_{ij}}^2(p) = C_{\dot{\varepsilon}_{ij}}(p,p)$. After some calculations, we find SNR to be

$$\mathrm{SNR}(p) = \frac{\mu_{||\dot{\varepsilon}||_{\mathrm{F}}}(p)}{\sigma_{||\dot{\varepsilon}||_{\mathrm{F}}}(p)} \tag{21}$$

$$= \frac{\mu_{\dot{\varepsilon}_{\mathrm{ee}}}(p)^2 + \mu_{\dot{\varepsilon}_{\mathrm{nn}}}(p)^2 + 2\mu_{\dot{\varepsilon}_{\mathrm{en}}}(p)^2}{\left(\sigma_{\dot{\varepsilon}_{\mathrm{ee}}}^2(p)\mu_{\dot{\varepsilon}_{\mathrm{ee}}}(p)^2 + \sigma_{\dot{\varepsilon}_{\mathrm{nn}}}^2(p)\mu_{\dot{\varepsilon}_{\mathrm{nn}}}(p)^2 + 4\sigma_{\dot{\varepsilon}_{\mathrm{en}}}^2(p)\mu_{\dot{\varepsilon}_{\mathrm{en}}}(p)^2\right)^{\frac{1}{2}}}. \tag{22}$$

We explicitly show that SNR is a function of p to emphasize that it identifies the position and time of anomalous deformation. We can reasonably suspect that some transient geophysical phenomena is occurring wherever and whenever SNR is larger than $\sim$3.

2.2 Outlier detection

In deriving our formulation for transient strain rates, we have assumed that noise in the data vector is normally distributed. This is not an appropriate assumption for GNSS data, which often have more outliers than would be expected for normally distributed noise. Methods for analyzing GNSS data should either be robust against outliers or should involve a preprocessing step in which outliers are detected and removed. Examples of the former include the MIDAS method for estimating secular velocities (Blewitt et al. 2016) and the GPS Imaging method for detecting spatially coherent features (Hammond et al. 2016). In this study, we identify and remove outliers as a preprocessing step before estimating $\dot{\varepsilon}$. Outliers are identified based on the residuals for a model that best fits the observed data. Observations with residuals that exceed some threshold are removed. This strategy for detecting outliers is commonly used for GNSS data, where the model being fit to the data typically consists of a linear trend and seasonal terms for each GNSS station (e.g., Johansson et al. 2002; Dong et al. 2006; Bos et al. 2013). To prevent transient geophysical signal from being erroneously identified as outliers, the model used in our outlier detection algorithm additionally consists of a temporally correlated Gaussian process. The details of our algorithm are given in Appendix A.

It should be noted that our algorithm does not identify jumps in GNSS time series, which are another common issue. Some, but not all, jumps can be automatically removed by looking up the dates of equipment changes and earthquakes (Gazeaux et al. 2013). However, it is still necessary to manually find and remove jumps of unknown origin.

3 APPLICATION TO PACIFIC NORTHWEST SLOW SLIP EVENTS

We use our method to estimate transient strain rates in the Pacific Northwest, and we are specifically interested in identifying strain resulting from SSEs (e.g., Dragert et al. 2001). In the Pacific Northwest, SSEs can be detected by monitoring for associated seismic tremor (Rogers & Dragert 2003), which is actively being done by the Pacific Northwest Seismic Network (Wech 2010). We can thus compare the tremor records to the transient strain rates estimated with GPR to verify that we are indeed identifying strain from SSEs.

We use the daily displacement solutions generated by the Geodesy Advancing Geosciences and EarthScope (GAGE) facility for continuous GNSS stations (Herring et al. 2016). This data is publicly available and can be found at www.unavco.org. We limit the dataset to the stations and time ranges which are pertinent to the seven most recent SSEs in the Puget Sound region. The earliest SSE considered in this study began in August 2010, and the most recent SSE began in February 2017. We use these most recent SSEs because the station coverage is sufficiently dense for us to use maximum likelihood methods to constrain prior models. The positions of GNSS stations used to estimate transient strain rates are shown in Figure 1.

3.1 Noise model

Before we determine the transient strain rates, we must establish a prior for the transient displacements, u, and the noise, η. In this section we discuss our choice for the noise covariance function C_η. There have been numerous studies on temporally correlated noise in GNSS data (e.g., Zhang et al. 1997; Mao et al. 1999; Williams et al. 2004; Langbein 2008). In these studies, temporally correlated noise was

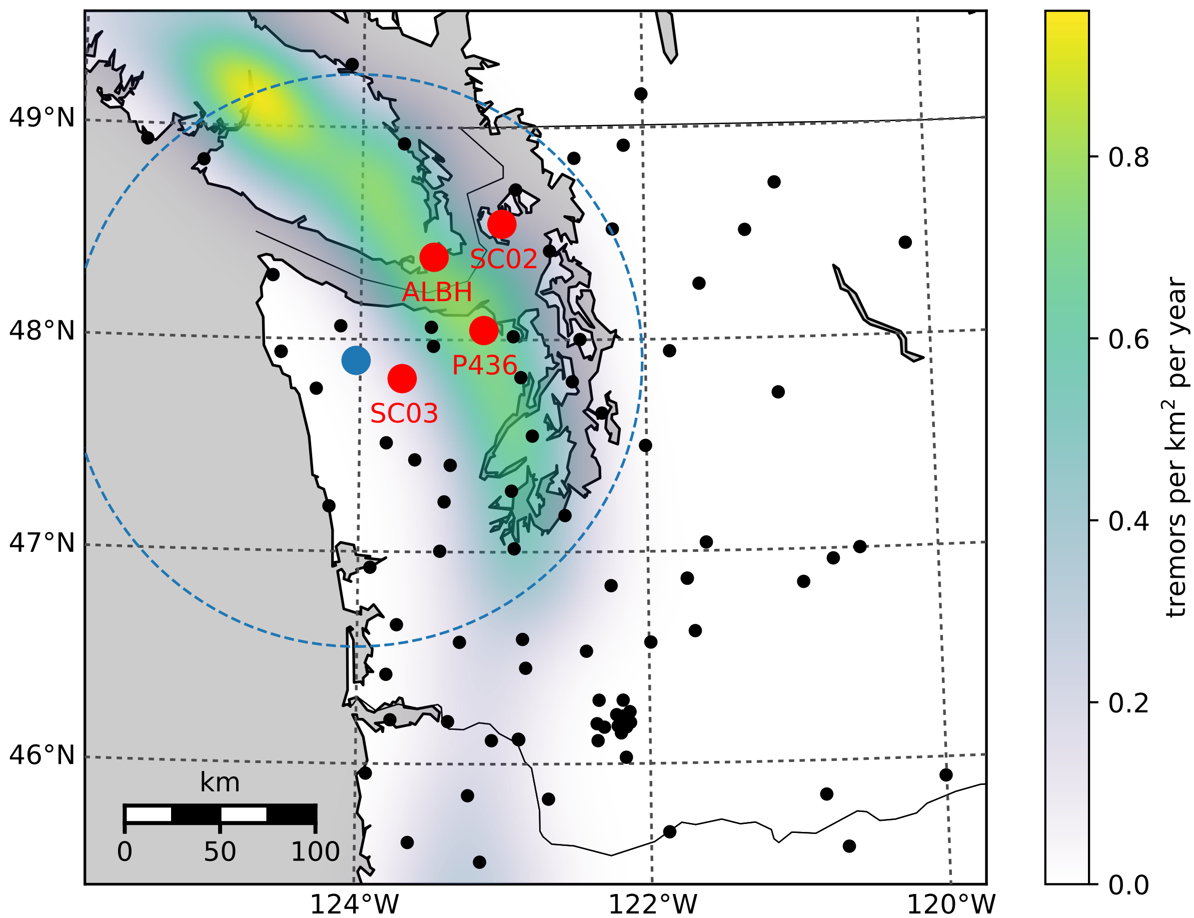

Figure 1. Positions of continuous GNSS stations used to estimate transient strain rates. The colored regions indicate the distribution of seismic tremor as determined by Wech (2010). The red dots show the positions of GNSS stations mentioned in this paper. The blue dot indicates the location of the transient strain rates shown in Figure 7 and the signal-to-noise ratio shown in Figure 8. The blue dashed circle demarcates the spatial extent of the tremors shown in Figure 8.

described with some combination of Brownian motion, a first-order Gauss-Markov (FOGM) process, and/or flicker noise. There is some physical justification for using Brownian motion as a noise model because it accurately describes the power spectrum of motion resulting from instability in geodetic monuments (e.g., Wyatt 1982, 1989). Here we describe the time dependence of η as a FOGM process and consider η to be spatially uncorrelated. A FOGM process is a solution to the stochastic differential equation

$$\dot{\eta}(t) + \alpha\eta(t) = \beta w(t), \tag{23}$$

where $w(t)$ is white noise with unit variance. The FOGM process degenerates to the commonly used Brownian motion noise model under the condition that $\alpha = 0$ and $\eta(0) = 0$. Our spatially uncorrelated noise model that satisfies eq. (23) is a Gaussian process with zero mean and the covariance function

$$C_\eta\left((\vec{x},t),(\vec{x}',t')\right) = \begin{cases} \frac{\beta^2}{2\alpha}\exp\left(-\alpha|t-t'|\right), & \vec{x} = \vec{x}' \\ 0, & \vec{x} \neq \vec{x}' \end{cases}. \tag{24}$$

We constrain the hyperparameters for η, α and β, with a set of 38 continuous GNSS stations in the Pacific Northwest that are east of 121°W. These stations are sufficiently far from the subduction zone that they are unlikely to contain transient signal associated with SSEs. We clean the data for these stations by removing jumps at times of equipment changes, and we remove outliers that have been detected with the algorithm described in Section 2.2. We then find α and β for each station time series with the Restricted Maximum Likelihood (REML) method (e.g., Harville 1974; Cressie 1993; Hines & Hetland 2017). The REML method finds the hyperparameters, which we collectively refer to as $\boldsymbol{\theta}$, that maximize the likelihood function

$$\mathcal{L}(\boldsymbol{\theta}) = \left(\frac{\left|\boldsymbol{G}^T\boldsymbol{G}\right|}{(2\pi)^{n-6m}\left|\boldsymbol{\Sigma}(\boldsymbol{\theta})\right|\left|\boldsymbol{G}^T\boldsymbol{\Sigma}(\boldsymbol{\theta})^{-1}\boldsymbol{G}\right|}\right)^{\frac{1}{2}} e^{-\frac{1}{2}\boldsymbol{d}_*^T\boldsymbol{K}(\boldsymbol{\theta})\boldsymbol{d}_*}, \tag{25}$$

where

$$\boldsymbol{K}(\boldsymbol{\theta}) = \boldsymbol{\Sigma}(\boldsymbol{\theta})^{-1} - \boldsymbol{\Sigma}(\boldsymbol{\theta})^{-1}\boldsymbol{G}\left(\boldsymbol{G}^T\boldsymbol{\Sigma}(\boldsymbol{\theta})^{-1}\boldsymbol{G}\right)^{-1}\boldsymbol{G}^T\boldsymbol{\Sigma}(\boldsymbol{\theta})^{-1}. \tag{26}$$

Harville (1974) showed that choosing the hyperparameters which maximize eq. (25) is equivalent to choosing the hyperparameters which maximize the probability of drawing $\boldsymbol{d}_*$ from $\boldsymbol{d}$. We use the REML method over the maximum likelihood method (e.g., Langbein & Johnson 1997) because the REML method accounts for the improper prior that we assigned to $\boldsymbol{a}$ (Hines & Hetland 2017). We independently estimate $\boldsymbol{\theta}$ for each station, and so $\boldsymbol{d}_*$ consists of displacements for an individual station. We are assuming $u(p) = 0$ when estimating the noise hyperparameters for this section. The distribution of inferred α and β are shown in Figure 2. The amplitude of FOGM noise, β, for the easting and northing components is notably low and are clustered around 0.5 mm/yr$^{0.5}$. The corresponding estimates of α tend to cluster around 0 yr^{-1}, suggesting that noise can be described with Brownian motion. We also estimate hyperparameters for the vertical component of displacements, under the hope that vertical deformation gradients could reveal some geophysical signal. The amplitude of FOGM noise for the vertical component is relatively large with a median value of 13.5 mm/yr$^{0.5}$. The inferred values for α are also higher for the vertical component with a median value of 8.21 yr^{-1}. In Figure 3, we use the median values of α and β to generate two random samples of FOGM noise for each component. The samples span five years and over these five years the easting and northing samples drift by about 1 mm. In the context of detecting SSEs, which produce several mm's of surface displace-

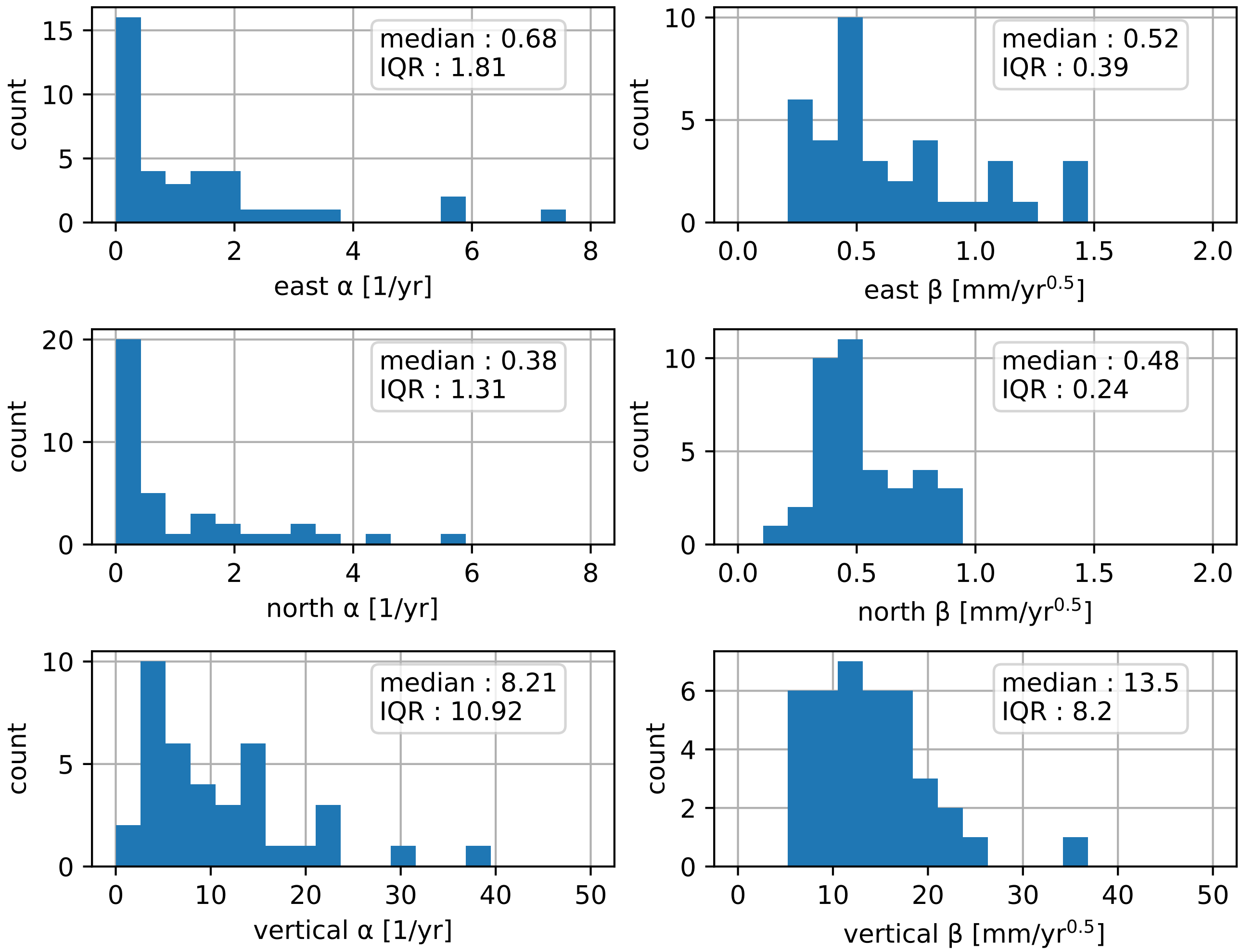

Figure 2. Distribution of estimated FOGM hyperparameters (eq. 24). Hyperparameters are estimated with the REML method for 38 stations in the Pacific Northwest that are east of 121°W. "IQR" is the interquartile range.

ment on the time-scale of weeks, the estimated FOGM noise for the easting and northing component is negligible. In contrast, the estimated FOGM noise for the vertical component is larger than the signal we would expect from SSEs. We suspect that the higher amplitude for the FOGM noise in the vertical component is accommodating for deficiencies in our rather simple seasonal model. Based on this analysis, we henceforth ignore temporally correlated noise in the easting and northing component because of its low amplitude. We also do not use vertical displacements because of the presumably low signal-to-noise ratio.

Another significant source of noise in GNSS data is common mode error (e.g., Wdowinski et al. 1997; Dong et al. 2006), which is noise that is highly spatially correlated. When not accounted for, common mode error manifests as spatially uniform undulations in estimated transient displacements.

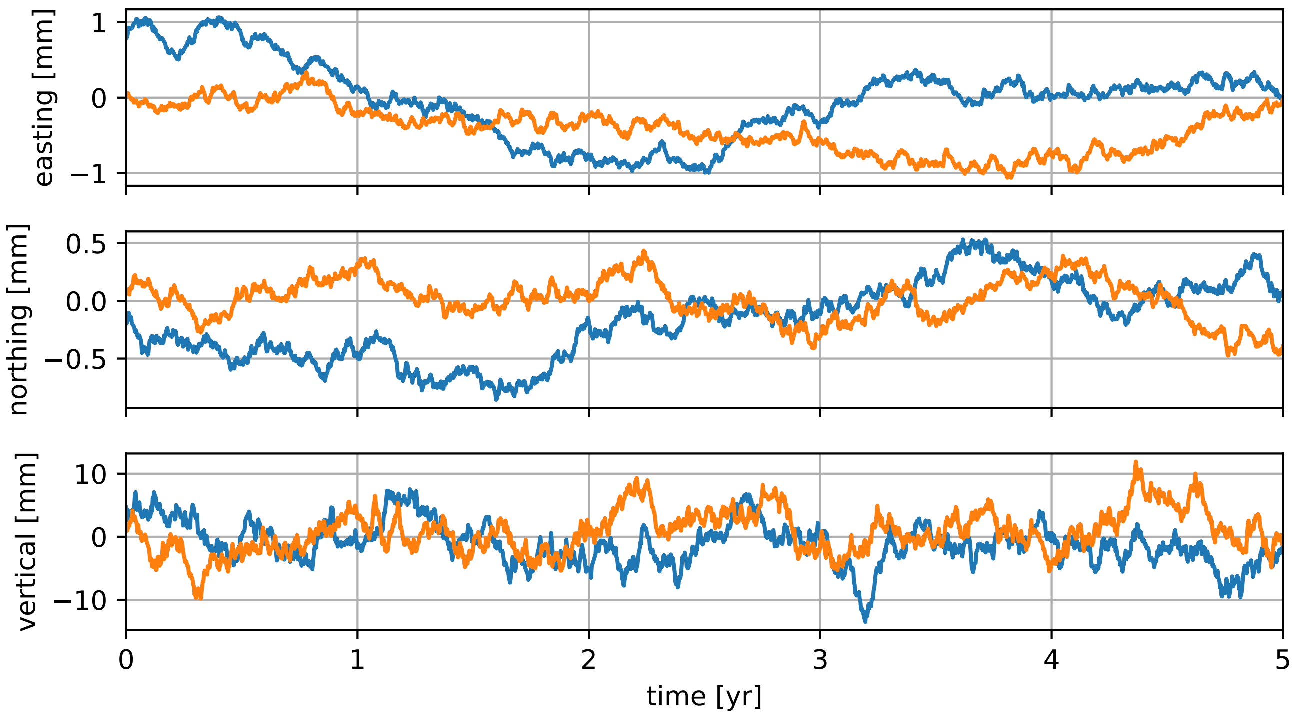

Figure 3. Two FOGM noise samples for each component. The FOGM hyperparameters have been set to the median values from Figure 2.

However, estimated transient strain rates are insensitive to common mode error. We therefore do not include common mode error in our noise model. We then make the simplifying assumption that $\eta(p) = 0$ for the easting and northing component of GNSS data.

3.2 Prior model

We next establish our prior model for transient displacements. Specifically, we discuss our choice for the covariance functions $X(\vec{x}, \vec{x}')$ and $T(t, t')$. For X, we use the squared exponential (SE) covariance function,

$$X(\vec{x}, \vec{x}') = \exp\left(\frac{-||\vec{x} - \vec{x}'||_2^2}{2\ell^2}\right). \tag{27}$$

The SE covariance function is commonly used in kriging (e.g, Cressie 1993) and Gaussian process regression (e.g., Rasmussen & Williams 2006). In terms of geodetic applications, Kato et al. (1998) and El-Fiky & Kato (1998) demonstrated that the SE accurately describes the covariance of secular GNSS derived velocities in Japan. The SE is a positive definite covariance function for any number of spatial dimensions. A Gaussian process with an SE covariance function is isotropic and has realizations that are infinitely differentiable.

We consider three potential models for the temporal covariance of u. First, we consider the one-dimensional SE covariance function,

$$T(t,t') = \phi^2 \exp\left(\frac{-|t-t'|^2}{2\tau^2}\right). \tag{28}$$

Note that T includes the hyperparameter ϕ, which serves to scale the covariance function C_u. Second, we consider integrated Brownian motion (IBM). IBM has zero mean and its covariance function can be found by integrating the covariance function for Brownian motion as

$$T(t,t') = \int_0^t \int_0^{t'} \phi^2 \min(s,s')\, ds'\, ds \tag{29}$$

$$= \frac{\phi^2}{2}\min(t,t')^2\left(\max(t,t') - \frac{1}{3}\min(t,t')\right), \quad t,t' \geq 0. \tag{30}$$

IBM has been used in the context of Kalman filtering as a non-parametric model for the time dependence of geophysical signals (e.g., Segall & Mathews 1997; McGuire & Segall 2003; Ohtani et al. 2010; Hines & Hetland 2016). It should be emphasized $t = 0$ is a reference time at which the Gaussian process is exactly zero. For some geophysical signals, it is appropriate to have this reference time. For example, if we are trying to identify postseismic deformation then t should be zero at the time of the earthquake. However, if we are interesting in detecting transient events, where there is no known start time, then IBM may not be an appropriate prior, and an isotropic Gaussian process should be preferred. In the following analysis, we make the quite arbitrary choice that t is zero on the first epoch of $\boldsymbol{d}_*$. Using an earlier reference time does not change the results discussed in this section. Our third option for T is the Wendland class of covariance functions (Wendland 2005). Wendland covariance functions have compact support and hence their corresponding covariance matrices are sparse. In our analysis, we exploit this sparsity with the CHOLMOD software package (Chen et al. 2008). Wendland functions are positive definite in $\mathbb{R}^d$, and they describes an isotropic Gaussian process with realizations that can be differentiated k times. The form of the covariance function depends on the choice of d and k. We use $d = 1$ since we are describing the temporal covariance of u. We use $k = 2$, giving samples of u continuous velocities and accelerations. The corresponding Wendland covariance function is

$$T(t,t') = \phi^2\left(1 - \frac{|t-t'|}{\tau}\right)_+^5 \left(\frac{8|t-t'|^2}{\tau^2} + \frac{5|t-t'|}{\tau} + 1\right), \tag{31}$$

where

$$(t)_+ = \begin{cases} t, & t > 0 \\ 0, & \text{otherwise.} \end{cases} \tag{32}$$

We next determine appropriate hyperparameters for X and each of the three candidate covariance functions for T. First, we clean the GNSS datasets by removing offsets at times of equipment changes and removing outliers with the method describe in Section 2.2. For the outlier detection algorithm, our

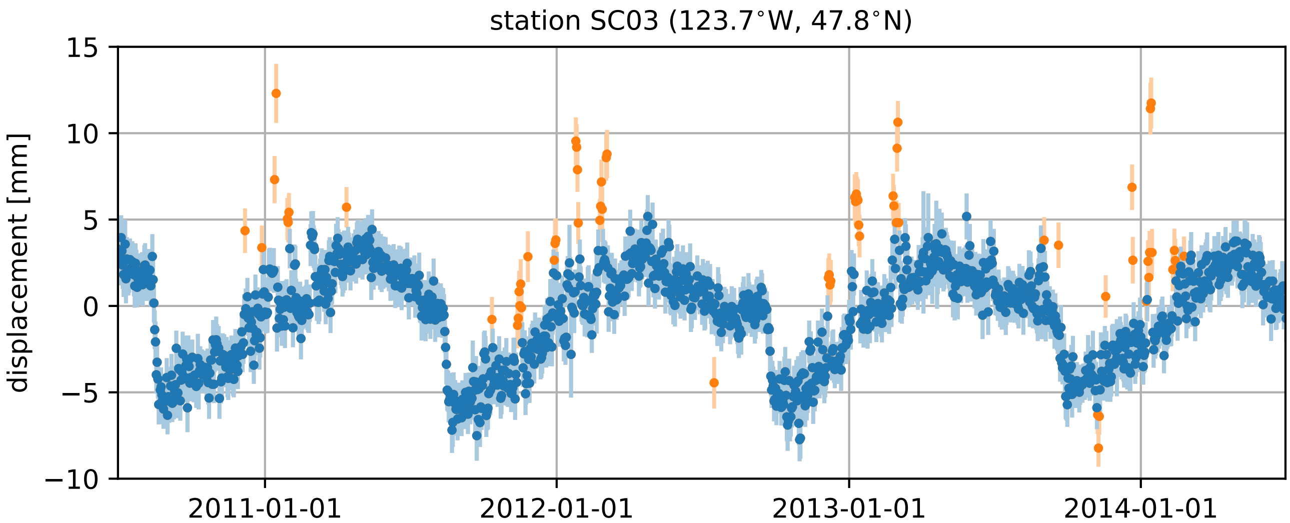

Figure 4. Detrended easting component of displacements at station SC03, which is located on Mount Olympus in Washington. The orange markers indicate outliers that were automatically detected using the algorithm from Section 2.2. The error bars show one standard deviation uncertainties. Note that outliers tend be observed in the winter, suggesting that they were caused by snow or ice.

prior model, u, is chosen to have a length-scale and time-scale that is able to approximately describe SSE displacements. We use the SE covariance function for X with length-scale $\ell = 100$ km, and we use the Wendland covariance function for T, due to its computational efficiency, with time-scale $\tau = 0.1$ yr and $\phi = 1$ mm. The outlier detection algorithm is particularly effective at removing outliers for stations at high elevation (Figure A1), which can be adversely affected by ice or snow during the winter (Lisowski et al. 2008). After cleaning the dataset, we divide it into seven subsets which are four months long and each centered on the time of a SSE. The times of the seven SSEs are determined with tremor records from Wech (2010). We use the REML method to find the optimal hyperparameters for T and X for each subset of data. We choose to make each data subsets four months long because it is long enough to encompass a SSE in the Pacific Northwest, while it is short enough to still be computationally tractable. However, four months is too short to resolve the sinusoids in $\boldsymbol{d}$, and they are omitted from $\boldsymbol{d}$ in this REML analysis for Pacific Northwest SSEs. The estimated hyperparameters for u are summarized in Table 1. Based on the interquartile ranges, the estimated hyperparameters for the SE and Wendland covariance functions do not vary significantly between SSEs. This suggests that the median of estimated hyperparameters should be an appropriate prior model for all Pacific Northwest SSEs. For the IBM model, there are several anomalously large values for ℓ and ϕ, which results in large interquartile ranges.

Next we identify which covariance function for T best describes the SSEs. One approach is to

Table 1. Optimal hyperparameters for the prior on transient displacements determined with the REML method. The temporal covariance function is indicated by the "T" column. The SE, IBM, and Wendland covariance functions are defined in eqs. (28), (29), and (31), respectively. The spatial covariance function, X, is the squared exponential (eq. 27) in all cases. The hyperparameters are estimated for each of the seven SSEs considered in this study, and the tabulated values indicate the median and interquartile ranges of estimates. The "diff $\log$(REML)" column compares the log REML likelihood to the log REML likelihood when using the SE covariance function for T. Negative values indicate that observations are more consistent with the SE covariance function.

T	direction	ℓ	ϕ	τ	diff. $\log$(REML)
SE	east	92 ± 25 km	0.62 ± 0.11 mm	0.026 ± 0.011 yr	-
SE	north	91 ± 53 km	0.43 ± 0.05 mm	0.030 ± 0.017 yr	-
Wendland	east	95 ± 30 km	0.66 ± 0.15 mm	0.093 ± 0.044 yr	0.78 ± 0.87
Wendland	north	92 ± 57 km	0.46 ± 0.10 mm	0.116 ± 0.057 yr	0.08 ± 0.58
IBM	east	110 ± 130 km	290 ± 420 mm/yr$^{1.5}$	-	-16.4 ± 7.8
IBM	north	150 ± 560 km	110 ± 250 mm/yr$^{1.5}$	-	-10.1 ± 2.3

compare the REML likelihoods for each covariance function, similar to the analysis in Langbein (2004). In Table 1, we summarize how the log REML likelihoods for the Wendland and IBM covariance functions compare to the SE covariance function. Based on the differences in log REML likelihoods, the data is substantially more likely to come from a Gaussian process with a SE or Wendland covariance function than an IBM covariance function. The REML likelihoods do not definitively indicate whether the SE or Wendland covariance function is preferable.

To further explore which covariance function for T best describes SSEs, we compare the observations to the predicted displacements for each covariance function. We consider the data prediction vector to be $\hat{\boldsymbol{d}} = (u(\boldsymbol{P}) + \boldsymbol{G}\boldsymbol{a})\,|\boldsymbol{d}_*$. Following a similar procedure as in Section 2, it can be shown that $\hat{\boldsymbol{d}}$ is normally distributed with mean

$$\boldsymbol{\mu}_{\hat{d}} = \begin{bmatrix} C_u(\boldsymbol{P},\boldsymbol{P}) & \boldsymbol{G} \end{bmatrix} \begin{bmatrix} \boldsymbol{\Sigma} & \boldsymbol{G} \\ \boldsymbol{G}^T & \boldsymbol{0} \end{bmatrix}^{-1} \begin{bmatrix} \boldsymbol{d}_* \\ \boldsymbol{0} \end{bmatrix} \tag{33}$$

and covariance

$$\boldsymbol{C}_{\hat{\boldsymbol{d}}} = C_u(\boldsymbol{P},\boldsymbol{P}) - \begin{bmatrix} C_u(\boldsymbol{P},\boldsymbol{P}) & \boldsymbol{G} \end{bmatrix} \begin{bmatrix} \boldsymbol{\Sigma} & \boldsymbol{G} \\ \boldsymbol{G}^T & \boldsymbol{0} \end{bmatrix}^{-1} \begin{bmatrix} C_u(\boldsymbol{P},\boldsymbol{P}) \\ \boldsymbol{G}^T \end{bmatrix}. \tag{34}$$

We compute $\hat{\boldsymbol{d}}$ using SE, Wendland, and IBM covariance functions for T and the median hyperparameters from Table 1. Figure 5 compares the easting component of $\boldsymbol{d}_*$ to $\hat{\boldsymbol{d}}$ during the winter 2015-2016 SSE at the three stations that record the strongest SSE signal, ALBH, P436, and SC02. Based on Figure 5, $\hat{\boldsymbol{d}}$ is insensitive to the choice of covariance function for T. The predicted displacements for the

IBM covariance function contain slightly more high frequency, and perhaps spurious, features. When comparing $\hat{\boldsymbol{d}}$ to $\boldsymbol{d}_*$ at station ALBH and SC02, it appears that $\hat{\boldsymbol{d}}$ slightly underestimates the rate of deformation during the SSE, regardless of the chosen covariance function. This over-smoothing could indicate that the chosen time-scale hyperparameter, τ, is too large. The predicted displacements at the remaining stations, which record more subtle SSE deformation, seem to faithfully describe $\boldsymbol{d}_*$.

For our estimates of transient strain discussed in the next section, we ultimately settle on the Wendland covariance function for T and use the median values from Table 1 for the hyperparameters. We choose the Wendland covariance function over the SE covariance function because of its computational advantages.

3.3 Transient Strain Rates

Having established a noise model and a prior for transient displacements, we use the cleaned GNSS dataset to calculate transient strain rates in the Puget Sound region. We calculate transient strain rates for each day from January 1, 2010 to May 15, 2017. The strain rates are estimates at a grid of points spanning the study area. In Figure 6 we show the transient strain rates on January 1, 2016, which coincides with the height of the winter 2015-2016 SSE. We have included an animation showing the map view of strain rates through time as supplementary material. The strain rates shown in Figure 6 are generally similar to the strain rates during the other six SSEs considered in this study. The SSEs cause trench perpendicular compression in the Olympic Peninsula and extension east of Puget Sound. The strain transitions from compression to extension around the southern tip of Vancouver Island, which coincides with the location of thrust slip for SSEs in the Puget Sound region (e.g., Dragert et al. 2001; Wech et al. 2009; Schmidt & Gao 2010). Thus, this pattern of strain is to be expected. During the period in between SSEs, secular strain rates indicate trench perpendicular compression throughout this study region (Murray & Lisowski 2000; McCaffrey et al. 2007, 2013). When comparing inferred strain rates from SSEs to the secular strain rates, we see that SSEs are concentrating tectonically accumulated strain energy towards the trench, and presumably pushing the subduction zone closer to failure.

In Figure 7 we show the time dependence of estimated transient strain rates at a position on the Olympic Peninsula, where transient strain rates from SSEs are largest. To verify that the estimated transient strain rates are accurately identifying geophysical signal, we compare the signal-to-noise ratio from eq. (21) to the frequency of seismic tremor (Figure 8). A signal-to-noise ratio greater than $\sim$3 can be interpreted as a detected geophysical signal. We detect nine distinct events, which each correspond to peaks in seismic tremor. The smaller events detected in August 2014 and February 2017 can be considered inter-SSE events. They were not among the SSEs used to constrain the prior covariance

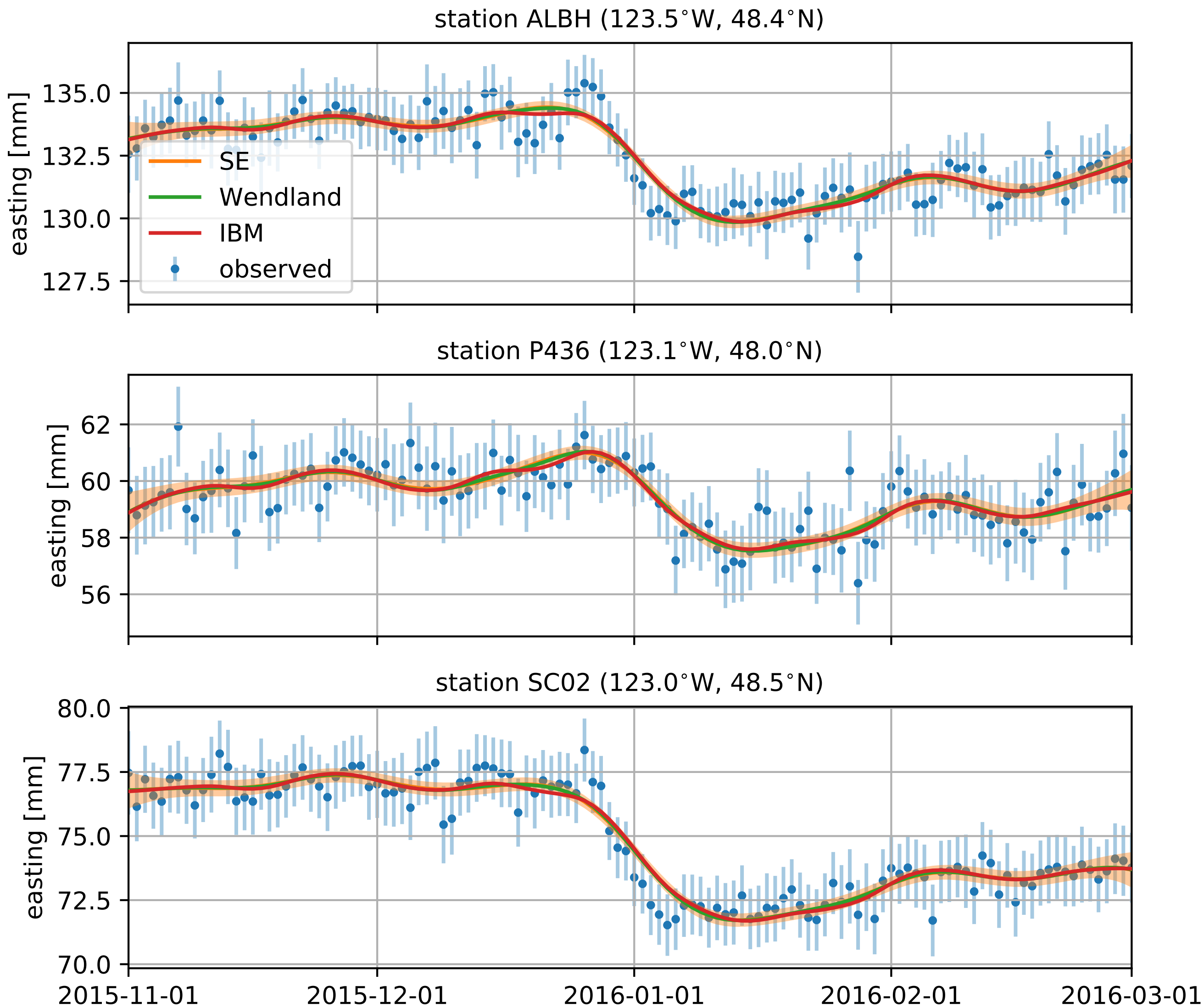

Figure 5. Easting component of the observed displacements, $\boldsymbol{d}_*$, and predicted displacements, $\hat{\boldsymbol{d}}$, during an SSE at three stations where the SSE signal is strongest. The predicted displacements are shown for when T is a squared exponential (SE), Wendland, and integrated Brownian motion (IBM) covariance function. The one standard deviation uncertainties are shown for the observations and the SE predictions. For clarity, uncertainties are not shown for the IBM and Wendland predictions, but they are nearly equivalent to the uncertainties for the SE predictions. The SE and Wendland predictions are practically indistinguishable.

function. In between peaks in seismic tremor, the signal-to-noise ratio is consistently between 0 and 2, suggesting that all the transient strain detected at this location is associated with SSEs and inter-SSE events.

The results we have presented thus far indicate that we are identifying the strain that we should expect to see. There are, however, subtle features in our estimated transient strain rates which we

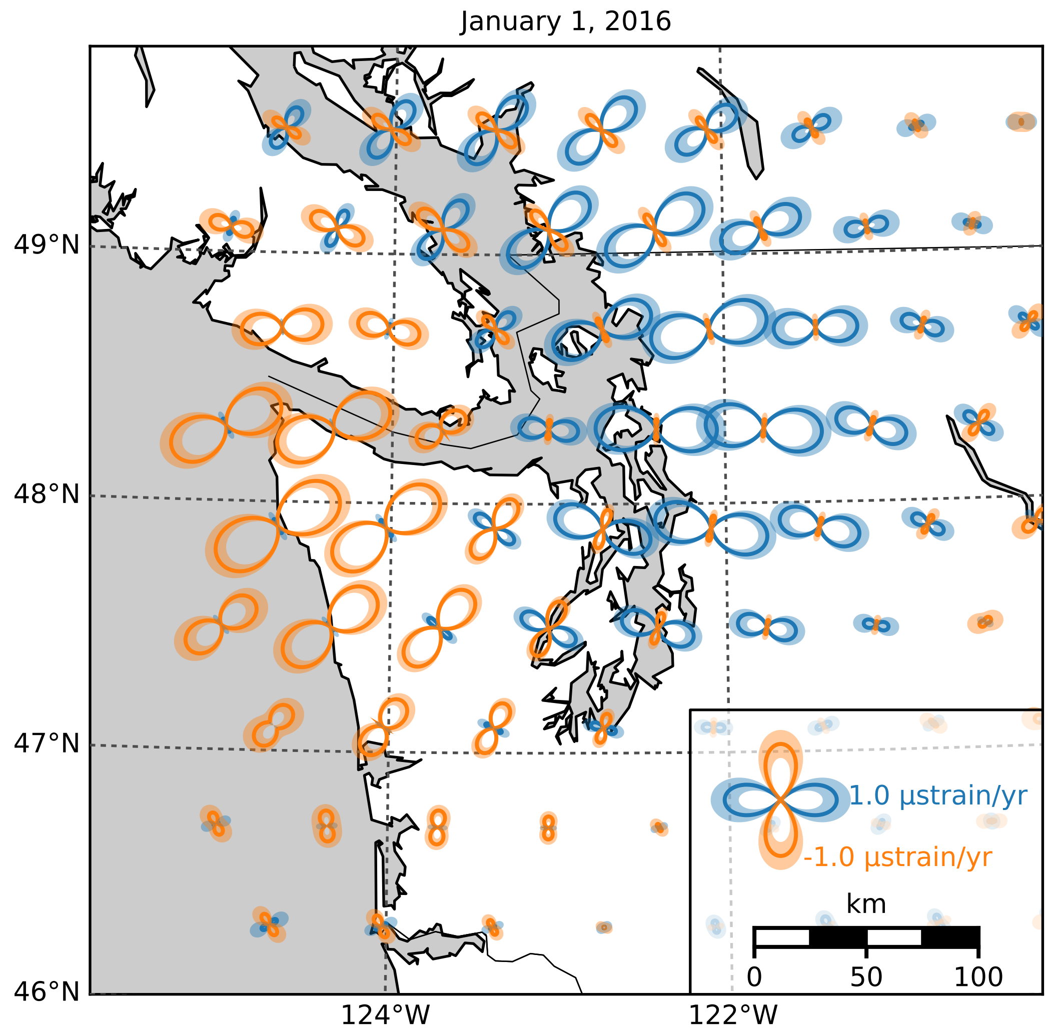

Figure 6. Estimated transient strain rates during the Winter 2015-2016 SSE. Strain glyphs show the normal strain rate along each azimuth, where orange indicates compression and blue indicates extension. The shaded regions indicate one standard deviation uncertainties in the normal strain rates.

were not expecting. For example, some SSEs are preceded by a brief period of east-west extension on the Olympic Peninsula. This feature can be seen several days before the summer 2012 and winter 2015-2016 SSEs in Figure 7 as well as in the supplementary animation. While this deformation is noteworthy, a discussion on the mechanisms causing it is outside the scope of this study.

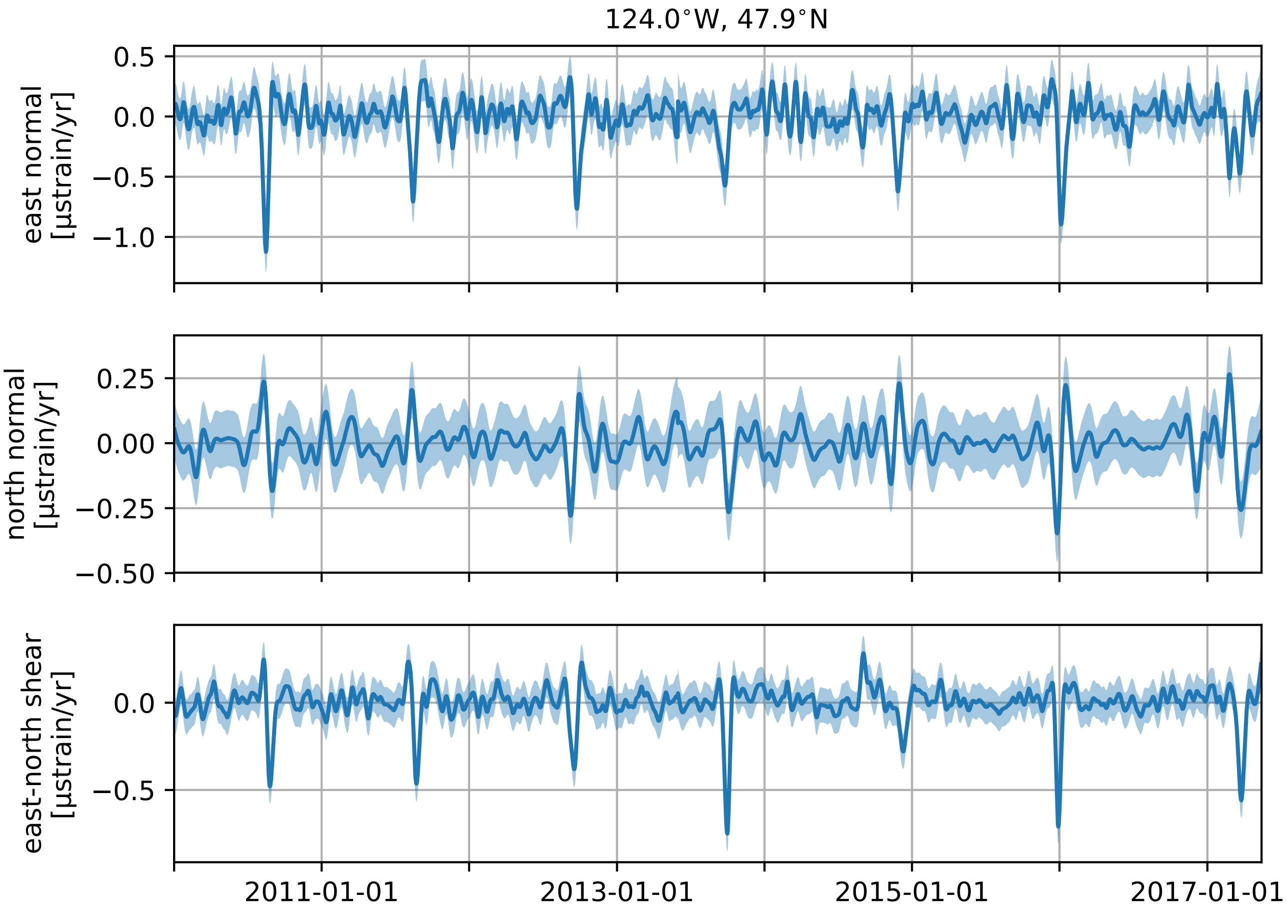

Figure 7. Three components of the transient horizontal strain rate tensor estimated at the position shown in Figure 1. The shaded regions indicate one standard deviation uncertainty.

4 DISCUSSION

Our results demonstrate that GPR is an effective tool for estimating transient strain from GNSS data, which can then be used to detect geophysical processes. One may argue that geophysical signal can also be detected by merely inspecting the GNSS displacement time series. Indeed, the SSEs identified in Figure 8 do produce visible displacements in the GNSS data. However, the GNSS data also contains outliers and non-tectonic deformation that is localized to individual stations. In contrast, our estimates of transient strain only identify features that are sufficiently spatially and temporally coherent, based on our chosen prior model. Furthermore, our estimates of transient strain are insensitive to common mode noise, which is highly spatially correlated noise resulting from factors such as reference frame error. Common mode noise can obscure geophysical signal in the GNSS data, but it gets canceled out when computing the transient strain. Lastly, our estimates of transient strain rates are a spatial and temporal derivative of displacements, and thus any geophysical signal in the transient strain rates tends

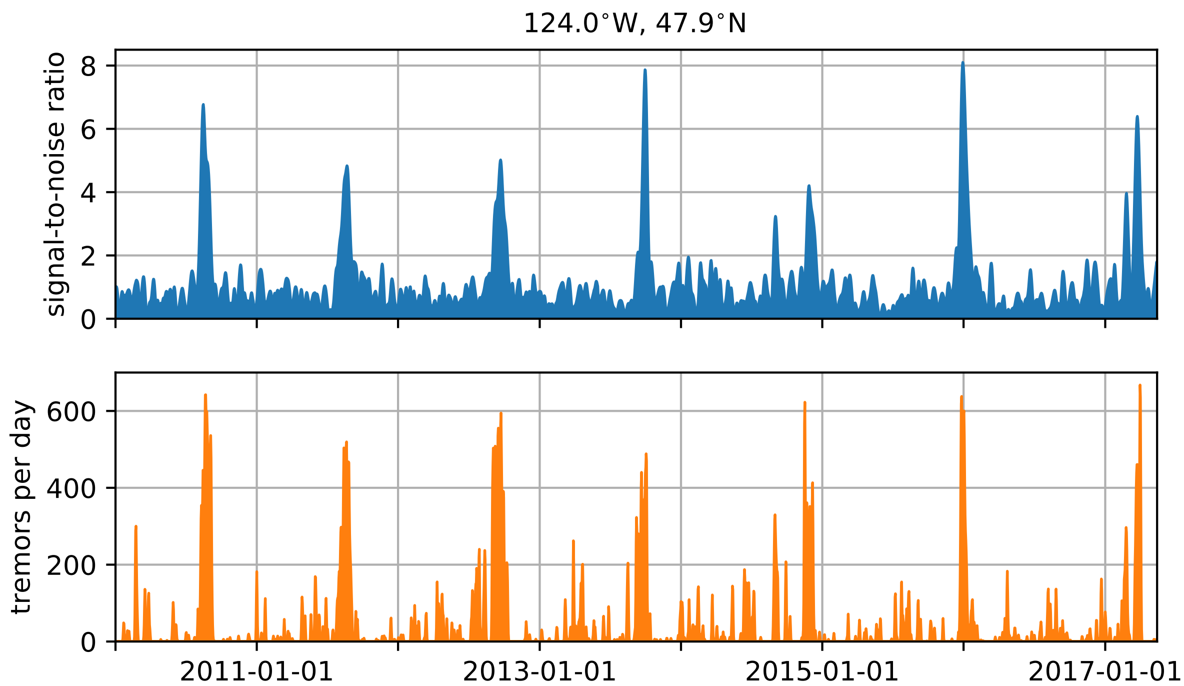

Figure 8. (top) Signal-to-noise ratio (eq. 21) at the position shown in Figure 1. (bottom) Frequency of tremors in the region shown in Figure 1.

to be more pronounced than in the GNSS data. For these reasons, we argue that transient strain rates estimated with the method described in Section 2 can illuminate geophysical signal that may not be discernible from the noise in the GNSS displacement data.

In addition to detecting geophysical processes, the GNSS derived transient strain rates can be used to better understand the data from borehole strain meters (BSMs). The Plate Boundary Observatory maintains about forty BSMs in the Pacific Northwest, and it has been demonstrated that BSMs are able to record transient geophysical events such as SSEs (e.g., Dragert & Wang 2011). However, there are complications that prevent BSM data from being used quantitatively in geophysical studies. One difficulty is that BSM data should be calibrated with a well known strain source, such as diurnal and semidiurnal tides (Hart et al. 1996; Roeloffs 2010; Hodgkinson et al. 2013). Unfortunately, the tidal forces at BSMs which record SSEs are strongly influenced by local bodies of water such as the Straight of Juan de Fuca, making it difficult to form a theoretical prediction of tidal strains (Roeloffs 2010). Another complication is that noise in BSM data is not well understood. The noise consists, in part, of a long-term decay resulting from the instrument equilibrating with the surrounding rock (Gladwin et al. 1987). Typically, this noise is dealt with in an ad-hoc manner by fitting and removing exponentials and low-order polynomials. We envision that the GNSS derived strain rates from this paper can be used as a reference strain for calibrating BSM data and quantify its noise.

There is potential for a more thorough analysis of the spatio-temporal noise in GNSS data, η, than what was performed in Section 3.1. We did not explore the spatial covariance of η, which would describe common mode noise. We are able to ignore common mode error in this study; however, for other geophysical studies based on GNSS data, such as fault slip inversions, it may be necessary to incorporate a spatially covarying noise model (e.g., Miyazaki et al. 2003). We can also improve upon the seasonal model used in this study, which consists of four spatially uncorrelated sinusoids for each station. We did not explore the spatial covariance of seasonal deformation or the temporal roughness (i.e., the number of sinusoids needed to describe the observations). The periodic Gaussian process (Mackay 1998) is an alternative model for seasonal deformation and is well suited for exploring the roughness of seasonal deformation. The periodic Gaussian process has zero mean and the covariance function

$$T(t,t') = \phi^2 \exp\left(\frac{-\sin(\pi|t-t'|)^2}{2\tau^2}\right). \tag{35}$$

Realizations have annual periodicity and the roughness is controlled by τ. Decreasing τ has the same effect as including higher frequency sinusoids in the seasonal model. The optimal value for τ can be found with the REML method as described in Section 3.1.

The transient strain rates estimated in this study are constrained by about seven years of daily displacement observations from 94 GNSS stations. It can be computationally intensive to evaluate eqs. (10) and (11) for a dataset with this size. We significantly reduce the amount of memory needed to estimate transient strain rates by describing the temporal covariance of displacements with a compact Wendland covariance function. Using a compact covariance function for our prior turns eqs. (10) and (11) into sparse systems of equations, which we then solve with CHOLMOD. CHOLMOD is designed for solving sparse, positive definite systems of equations. The matrix being inverted in eqs. (10) and (11) is not positive definite; however, we can use another partitioned matrix inversion identity from Press et al. (2007) to partition it into positive definite submatrices to be inverted. Even when using a compact covariance function, it may still be necessary to reduce the computational burden by dividing the data into subsets and evaluating transient strain rates for each subset.

5 CONCLUSION

In this paper we propose using Gaussian process regression (GPR) to estimate transient strain rates from GNSS data. Most other methods for estimating strain rates assume a parametric representation of deformation, which can bias the results if the parameterization is not chosen carefully. Here we assume a stochastic, rather than parametric, prior model for displacements. Our prior model describes how much we expect transient displacements to covary spatially and temporally. If we know nothing about the underlying signal that we are trying to recover, then the prior model can be chosen objectively with maximum likelihood methods. Because GPR is a Bayesian method, the uncertainties on our estimated transient strain rates are well quantified, allowing one to discern geophysical signal from noise. We demonstrate that GPR is an effective tool for detecting geophysical phenomena, such as slow slip events, in our application to GNSS data from the Pacific Northwest. One limitation with GPR is that it is not robust against outliers. To overcome this limitation, we have introduced an effective pre-processing method for identifying and removing outliers from GNSS datasets. Another complication with GPR is that it usually involves inverting a dense matrix where the number of rows and columns is equal to the number of observations. This is prohibitive when using several years of daily GNSS observations from a network of several hundred stations. We significantly reduce the computational burden of GPR by using compact Wendland covariance function to describe our prior model. While this paper just focuses on estimating transient strain rates, we believe that GPR is a powerful tool that can be applied to a wide range of geophysical problems.

6 ACKNOWLEDGEMENTS

This material is based upon work supported by the National Science Foundation under grant EAR 1245263. The EarthScope Plate Boundary Observatory data is provided by UNAVCO through the GAGE Facility with support from the National Science Foundation (NSF) and National Aeronautics and Space Administration (NASA) under NSF Cooperative Agreement EAR-1261833. An implementation of the method described in this paper is named Python-based Geodetic Network Strain software (PyGeoNS). PyGeoNS is distributed under the MIT License and can be found at www.github.com/treverhines/PyGeoNS.

APPENDIX A: OUTLIER DETECTION ALGORITHM

Our outlier detection algorithm is loosely based on the data editing algorithm from Acheson (1975). Let $\boldsymbol{d}^*$ denote all n GNSS displacement observations for a single directional component, which have been made at positions and times $\boldsymbol{P}$. We describe $\boldsymbol{d}^*$ as a realization of the random vector

$$\boldsymbol{d} = \boldsymbol{G}\boldsymbol{m} + v(\boldsymbol{P}) + \boldsymbol{w}, \tag{A.1}$$

where $\boldsymbol{G}$ and $\boldsymbol{m}$ are the same as in eq. (4), v is a Gaussian process distributed as $\mathcal{GP}(0, C_v)$, and $\boldsymbol{w}$ is a vector of uncorrelated Gaussian noise with known standard deviations $\boldsymbol{\sigma} = [\sigma_1, \sigma_2, ..., \sigma_n]$. The Gaussian process v is intended to describe transient features in the data that cannot be explained by the linear trend or seasonal terms in $\boldsymbol{G}$. We let the temporal covariance of v be a squared exponential, and we let v be spatially uncorrelated so that,

$$C_v(p,p') = \phi^2 \exp\left(\frac{-|t-t'|^2}{2\tau^2}\right)\delta_{\vec{x},\vec{x}'}, \tag{A.2}$$

where $\delta_{\vec{x},\vec{x}'} = 1$ if $\vec{x} = \vec{x}'$ and 0 otherwise. The spatial covariance of v has little effect on the detected outliers, and so we have assumed that v is spatially uncorrelated for simplicity. Based on our experience, v can reasonably describe most transient features in the data when we set $\phi = 1$ mm and $\tau = 10$ days.

Our goal is to find the index set of non-outliers in $\boldsymbol{d}^*$, which we denote as $\boldsymbol{\Omega}$. We use a tilde to indicate that an array only contains elements corresponding to $\boldsymbol{\Omega}$ (e.g., the vector of non-outlier observations is denoted $\tilde{\boldsymbol{d}}^* = [d_i^*]_{i\in\boldsymbol{\Omega}}$). The outliers are identified iteratively, and we initiate $\boldsymbol{\Omega}$ with all n indices. We consider outliers to be data that are poorly explained by the model $\boldsymbol{Gm} + v(\boldsymbol{P})$, which is determine by the residual vector

$$\begin{aligned}\boldsymbol{r} &= \boldsymbol{d}^* - \mathrm{E}\left[\left(\boldsymbol{Gm} + v(\boldsymbol{P})\right)\Big|\left(\tilde{\boldsymbol{d}} = \tilde{\boldsymbol{d}}^*\right)\right] \\ &= \boldsymbol{d}^* - \begin{bmatrix} C_v(\boldsymbol{P},\tilde{\boldsymbol{P}}) & \boldsymbol{G} \end{bmatrix} \begin{bmatrix} C_v(\tilde{\boldsymbol{P}},\tilde{\boldsymbol{P}}) + \mathrm{diag}(\tilde{\boldsymbol{\sigma}}^2) & \tilde{\boldsymbol{G}} \\ \tilde{\boldsymbol{G}}^T & \boldsymbol{0} \end{bmatrix}^{-1} \begin{bmatrix} \tilde{\boldsymbol{d}}^* \\ \boldsymbol{0} \end{bmatrix}.\end{aligned} \tag{A.3}$$

Data with abnormally large residuals are identified as outliers. For each iteration, we compute $\boldsymbol{r}$ and then update $\boldsymbol{\Omega}$ so that it contains the indices of $\boldsymbol{r}$ whose weighted values are less than λ times the weighted root mean square of $\tilde{\boldsymbol{r}}$,

$$\boldsymbol{\Omega} \leftarrow \left\{ i : \left|\frac{r_i}{\sigma_i}\right| < \lambda \cdot \sqrt{\frac{1}{|\boldsymbol{\Omega}|}\sum_{j\in\boldsymbol{\Omega}} \frac{r_j^2}{\sigma_j^2}} \right\}. \tag{A.4}$$

Iterations continue until the new $\boldsymbol{\Omega}$ is the same as the previous $\boldsymbol{\Omega}$.

The outlier detection algorithm is demonstrated in Figure A1. For the demonstration, we use the easting component of displacements at a single station, SC03, which is located on Mt. Olympus in Washington state. Station SC03 records anomalous observations during the winter, presumably because of snow and ice accumulation, and we want to remove these observations. The station also records periodic westward motion from slow slip events, and we want to keep this deformation intact. The detected outliers are shown in Panel B. For comparison, we also show the detected outliers when we do not include the Gaussian process v in our model for the data (Panel A). When v is not included, real transient deformation resulting from slow slip events is erroneously identified as outliers. When v is included, the identified outliers only consist of the anomalous deformation that lacks temporal continuity. It should be noted that we use $\lambda = 2.5$ for this demonstration, which causes the outlier

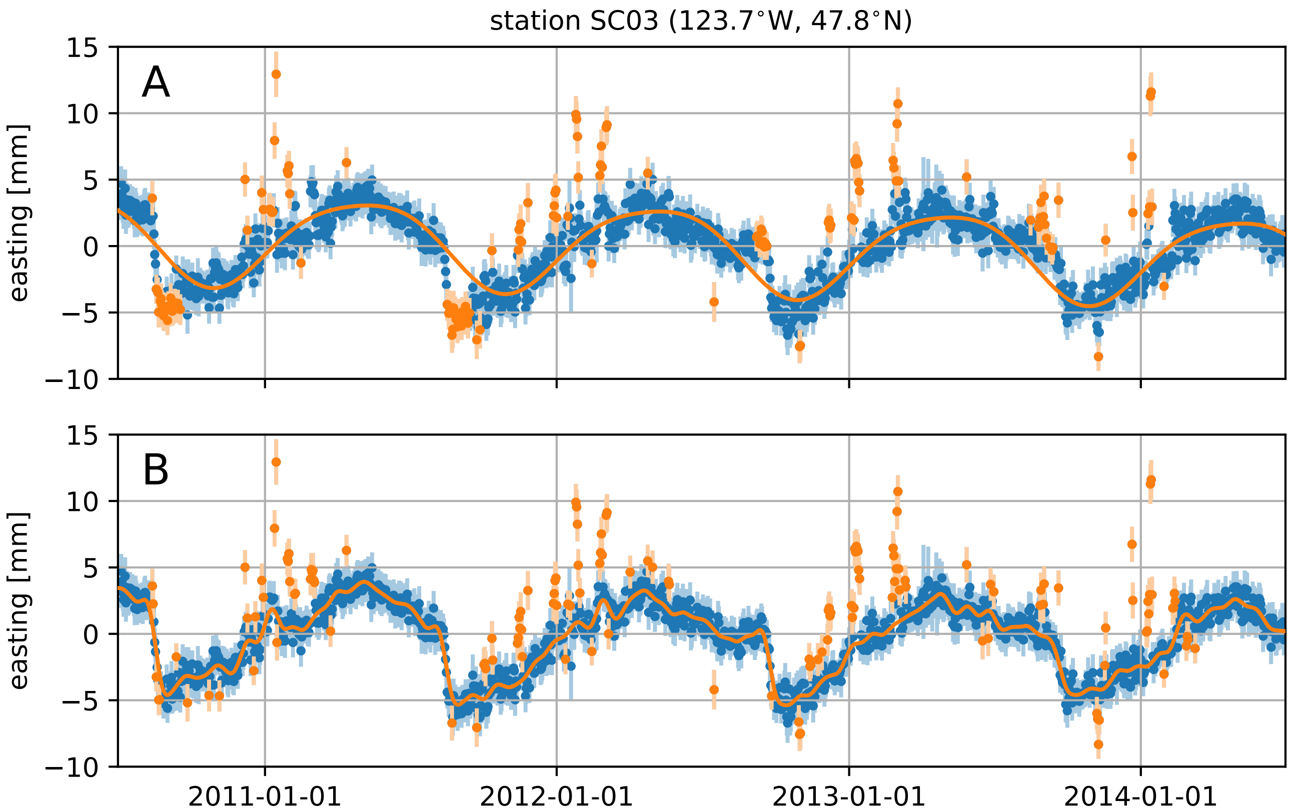

Figure A1. Outliers detected in the easting component of displacements at station SC03. The orange markers indicate detected outliers. The orange line is the best fit model to the data, which is used to compute the residual vector $\boldsymbol{r}$. The model being fit to the data in Panel A is $\boldsymbol{Gm}$, and the model in Panel B is $\boldsymbol{Gm} + v(\boldsymbol{P})$.

detection algorithm to be particularly aggressive. In Section 3, we clean the data using a more tolerant $\lambda = 4.0$.

REFERENCES

Acheson, D. T., 1975. Data editing - subroutine editq, Tech. rep., US Department of Commerce, National Oceanic and Atmospheric Administration, Environmental Data Service.

Adler, R. J., 1981. *The Geometry of Random Fields*, John Wiley & Sons, Chichester.

Beavan, J. & Haines, J., 2001. Contemporary horizontal velocity and strain rate fields of the Pacific-Australian plate boundary zone through New Zealand, *Journal of Geophysical Research*, **106**(B1), 741–770.

Blewitt, G., Kreemer, C., Hammond, W. C., & Gazeaux, J., 2016. MIDAS robust trend estimator for accurate GPS station velocities without step detection, *Journal of Geophysical Research : Solid Earth*, **121**, 2054–2068.

Bos, M. S., Fernandes, R. M. S., Williams, S. D. P., & Bastos, L., 2013. Fast error analysis of continuous GNSS observations with missing data, *Journal of Geodesy*, **87**(4), 351–360.

Chen, Y., Davis, T. a., & Hager, W. W., 2008. Algorithm 887 : CHOLMOD , Supernodal Sparse Cholesky Factorization and Update/downdate, *ACM Transactions on Mathematical Software*, **35**(3), 1–12.

Cressie, N., 1993. *Statistics for Spatial Data*, John Wiley & Sons, New York, rev. edn.

Dong, D., Fang, P., Bock, Y., Cheng, M. K., & Miyazaki, S., 2002. Anatomy of apparent seasonal variations from GPS-derived site position time series, *J. Geophys. Res.*, **107**(B4), 2075.

Dong, D., Fang, P., Bock, Y., Webb, F., Prawirodirdjo, L., Kedar, S., & Jamason, P., 2006. Spatiotemporal filtering using principal component analysis and Karhunen-Loeve expansion approaches for regional GPS network analysis, *Journal of Geophysical Research: Solid Earth*, **111**(3), 1–16.

Dragert, H. & Wang, K., 2011. Temporal evolution of an episodic tremor and slip event along the northern Cascadia margin, *Journal of Geophysical Research: Solid Earth*, **116**(12), 1–12.

Dragert, H., Wang, K., & James, T. S., 2001. A silent slip event on the deeper Cascadia subduction interface., *Science*, **292**, 1525–1528.

El-Fiky, G. S. & Kato, T., 1998. Continuous distribution of the horizontal strain in the Tohoku district, Japan, predicted by least-squares collocation, *Journal of Geodynamics*, **27**(2), 213–236.

Feigl, K. L., King, R. W., & Jordan, T. H., 1990. Geodetic measurement of tectonic deformation in the Santa Maria Fold and Thrust Belt, California, *Journal of Geophysical Research: Solid Earth*, **95**(B3), 2679–2699.

Field, E. H., Arrowsmith, R. J., Biasi, G. P., Bird, P., Dawson, T. E., Felzer, K. R., Jackson, D. D., Johnson, K. M., Jordan, T. H., Madden, C., Michael, A. J., Milner, K. R., Page, M. T., Parsons, T., Powers, P. M., Shaw, B. E., Thatcher, W. R., Weldon, R. J., & Zeng, Y., 2014. Uniform California Earthquake Rupture Forecast, version 3 (UCERF3) -The time-independent model, *Bulletin of the Seismological Society of America*, **104**(3), 1122–1180.

Freed, a. M. & Lin, J., 2001. Delayed triggering of the 1999 Hector Mine earthquake by viscoelastic stress transfer., *Nature*.

Gazeaux, J., Williams, S., King, M., Bos, M., Dach, R., Deo, M., Moore, A. W., Ostini, L., Petrie, E., Roggero, M., Teferle, F. N., Olivares, G., & Webb, F. H., 2013. Detecting offsets in GPS time series: First results from the detection of offsets in GPS experiment, *Journal of Geophysical Research: Solid Earth*, **118**(5), 2397–2407.

Gladwin, M. T., Gwyther, R. L., Hart, R., Francis, M., & Johnston, M. J. S., 1987. Borehole tensor strain measurements in California, *Journal of Geophysical Research: Solid Earth*, **92**(B8), 7981–7988.

Hammond, W. C., Blewitt, G., & Kreemer, C., 2016. GPS imaging of vertical land motion in California and Nevada: Implications for Sierra Nevada uplift, *Journal of Geophysical Research : Solid Earth*.

Hart, R. H. G., Gladwin, M. T., Gwyther, R. L., Agnew, D. C., & Wyatt, F. K., 1996. Tidal calibration of borehole strain meters: Removing the effects of small-scale inhomogeneity, *Journal of Geophysical Research*, **101**(96).

Harville, D. A., 1974. Bayesian Inference for Variance Components Using Only Error Contrasts, *Biometrika*,

61(2), 383–385.

Hastie, T., Tibshirani, R., & Friedman, J., 2009. *The Elements of Statistical Learning: Data Mining, Inference, and Prediction*, Springer-Verlag, 2nd edn.

Herring, T. A., Melbourne, T. I., Murray, M. H., Floyd, M. A., Szeliga, W. M., King, R. W., Phillips, D. A., Puskas, C. M., Santillan, M., & Wang, L., 2016. Plate Boundary Observatory and related networks: GPS data analysis methods and geodetic product, *Reviews of Geophysics*, pp. 1–50.

Hines, T. T. & Hetland, E. A., 2016. Rheologic constraints on the upper mantle from five years of postseismic deformation following the El Mayor-Cucapah earthquake, *Journal of Geophysical Research: Solid Earth*, **121**.

Hines, T. T. & Hetland, E. A., 2017. Unbiased characterization of noise in geodetic data, *submitted to Journal of Geodesy*.

Hodgkinson, K., Agnew, D., & Roeloffs, E., 2013. Working With Strainmeter Data, *Eos, Transactions American Geophysical Union*, **94**(9), 91–91.

Holt, W. E. & Shcherbenko, G., 2013. Toward a Continuous Monitoring of the Horizontal Displacement Gradient Tensor Field in Southern California Using cGPS Observations from Plate Boundary Observatory (PBO), *Seismological Research Letters*, **84**(3), 455–467.

Johansson, J. M., Davis, J. L., Scherneck, H., Milne, G. A., Vermeer, M., Mitrovica, J. X., Bennett, R. A., Jonsson, B., Elgered, G., Elo, P., & Koivula, H., 2002. Continuous GPS measurements of postglacial adjustment in Fennoscandia 1. Geodetic results, *Journal of Geophysical Research*, **107**.

Kato, T., El-Fiky, G. S., Oware, E. N., & Miyazaki, S., 1998. Crustal strains in the Japanese islands as deduced from dense GPS array, *Geophysical Research Letters*, **25**(18), 3445–3448.

Langbein, J., 2004. Noise in two-color electronic distance meter measurements revisited, *Journal of Geophysical Research: Solid Earth*, **109**(4), 1–16.

Langbein, J., 2008. Noise in GPS displacement measurements from Southern California and Southern Nevada, *Journal of Geophysical Research: Solid Earth*, **113**(5), 1–12.

Langbein, J. & Johnson, H., 1997. Correlated errors in geodetic time series: Implications for time-dependent deformation, *Journal of Geophysical Research*, **102**(B1), 591–603.

Lisowski, M., Dzurisin, D., Denlinger, R. P., & Iwatsubo, E. Y., 2008. Analysis of GPS-Measured Deformation Associated with the 2004 2006 Dome-Building Eruption of Mout St. Helens, Washington, Tech. Rep. September 1984.

Lohman, R. B. & Murray, J. R., 2013. The SCEC Geodetic Transient-Detection Validation Exercise, *Seismological Research Letters*, **84**(3), 419–425.

Mackay, D. J. C., 1998. Introduction to Gaussian processes, *Neural Networks and Machine Learning*, **168**(1996), 133–165.

Mao, A., Harrison, G. A., & Dixon, H., 1999. Noise in GPS coordinate time series, *Journal of Geophysical Research*, **104**(B2), 2797–2816.

McCaffrey, R., Qamar, A. I., King, R. W., Wells, R., Khazaradze, G., Williams, C. A., Stevens, C. W., Vollick,

J. J., & Zwick, P. C., 2007. Fault locking, block rotation and crustal deformation in the Pacific Northwest, *Geophysical Journal International*, **169**(3), 1315–1340.

McCaffrey, R., King, R. W., Payne, S. J., & Lancaster, M., 2013. Active tectonics of northwestern U.S. inferred from GPS-derived surface velocities, *Journal of Geophysical Research: Solid Earth*, **118**, 709–723.

McGuire, J. J. & Segall, P., 2003. Imaging of aseismic fault slip transients recorded by dense geodetic networks, *Geophysical Journal International*, **155**, 778–788.

Meade, B. J. & Hager, B. H., 2005. Block models of crustal motion in southern California constrained by GPS measurements, *Journal of Geophysical Research: Solid Earth*, **110**, 1–19.

Miyazaki, S., McGuire, J. J., & Segall, P., 2003. A transient subduction zone slip episode in southwest Japan observed by the nationwide GPS array, *Journal of Geophysical Research*, **108**(B2), 1–15.

Moritz, H., 1978. Least-Squares Collocation, *Reviews of Geophysics*, **16**(3), 421–430.

Murray, M. H. & Lisowski, M., 2000. Strain accumulation along the Cascadia subduction zone in western Washington, *Geophysical Research Letters*, **27**(22), 3631–3634.

Ohtani, R., McGuire, J. J., & Segall, P., 2010. Network strain filter: A new tool for monitoring and detecting transient deformation signals in GPS arrays, *Journal of Geophysical Research: Solid Earth*, **115**(12), 1–17.

Okada, Y., 1992. Internal deformation due to shear and tensile faults in a half space, *Bulletin of the Seismological Society of America*, **82**(2), 1018–1040.

Papoulis, A., 1991. *Probability, Random Variables, and Stochastic Processes*, McGraw-Hill, New York, 3rd edn.

Press, W. H., Flannery, B. P., Teukolsky, S. A., & Vetterling, W. T., 2007. *Numerical Recipes: The Art of Scientific Computing*, Cambridge University Press, Cambridge, 3rd edn.

Rasmussen, C. E. & Williams, C. K. I., 2006. *Gaussian processes for machine learning*, The MIT Press.

Roeloffs, E., 2010. Tidal calibration of Plate Boundary Observatory borehole strainmeters: Roles of vertical and shear coupling, *Journal of Geophysical Research: Solid Earth*, **115**(6), 1–25.

Roeloffs, E. A., 2006. Evidence for Aseismic Deformation Rate Changes Prior To Earthquakes, *Annual Review of Earth and Planetary Sciences*, **34**(1), 591–627.

Rogers, G. & Dragert, H., 2003. Episodic tremor and slip on the Cascadia subduction zone: the chatter of silent slip., *Science*, **300**, 1942–1943.

Sandwell, D. T. & Wessel, P., 2016. Interpolation of 2-D vector data using constraints from elasticity, *Geophysical Research Letters*, pp. 1–7.

Schmidt, D. A. & Gao, H., 2010. Source parameters and time-dependent slip distributions of slow slip events on the Cascadia subduction zone from 1998 to 2008, *Journal of Geophysical Research: Solid Earth*, **115**(4), 1–13.

Segall, P. & Mathews, M., 1997. Time dependent inversion of geodetic data, *Journal of Geophysical Research*, **102**(B10), 22391–22409.

Shen, Z., Wang, M., Zeng, Y., & Wang, F., 2015. Optimal Interpolation of Spatially Discretized Geodetic Data, *Bulletin of the Seismological Society of America*, **105**(4), 2117–2127.

Shen, Z. K., Jackson, D. D., Ge, B. X., & Bob, X. G., 1996. Crustal deformation across and beyond the Los Angeles basin from geodetic measurements, *Journal of Geophysical Research*, **101**(B12), 27927–27957.

Tape, C., Musé, P., Simons, M., Dong, D., & Webb, F., 2009. Multiscale estimation of GPS velocity fields, *Geophysical Journal International*, **179**(2), 945–971.

von Mises, R., 1964. *Mathematical Theory of Probability and Statistics*, Academic Press, New York.

Wdowinski, S., Zhang, J., Fang, P., & Genrich, J., 1997. Southern California Permanent GPS Geodetic Array: Spatial filtering of daily positions for estimating coseismic and postseismic displacements induced by the 1992 Landers earthquake, **102**(97), 57–70.

Wech, A. G., 2010. Interactive Tremor Monitoring, *Seismological Research Letters*, **81**(4), 664 – 669.

Wech, A. G., Creager, K. C., & Melbourne, T. I., 2009. Seismic and geodetic constraints on Cascadia slow slip, *Journal of Geophysical Research: Solid Earth*, **114**(10), 1–9.

Wendland, H., 2005. *Scattered data approximation*.

Williams, S. D. P., Bock, Y., Fang, P., Jamason, P., Nikolaidis, R. M., Prawirodirdjo, L., Miller, M., & Johnson, D. J., 2004. Error analysis of continuous GPS position time series, *Journal of Geophysical Research: Solid Earth*, **109**(B3).

Wyatt, F., 1982. Displacement of Surface Monuments: Horizontal Motion, *Journal of Geophysical Research*, **87**(B2), 979–989.

Wyatt, F. K., 1989. Displacement of surface monuments: Vertical motion, *Journal of Geophysical Research*, **94**(B2), 1655–1664.

Zhang, J., Bock, Y., Johnson, H., Fang, P., Williams, S., Genrich, J., Wdowinski, S., & Behr, J., 1997. Southern California Permanent GPS Geodetic Array: Error analysis of daily position estimates and site velocities, *Journal of Geophysical Research*, **102**(B8), 18035–18055.